Journal of Electronic Materials (2023) 52:1484–1492
https://doi.org/10.1007/s11664-022-10104-z

ORIGINAL RESEARCH ARTICLE

Effects of Pre-Metallization on the MOCVD Growth and Properties of Ge-doped AlGaN on AlN/Sapphire Templates

Timothy Mirabito[1] · Ke Wang[2] · Joan M. Redwing[1,2]

Received: 21 June 2022 / Accepted: 15 November 2022 / Published online: 12 December 2022

Abstract
The effects of pre-metallization of the growth surface on film stress and structural properties of undoped and Ge-doped $Al_xGa_{1-x}N$ ($x \sim 0.5$–0.6) epilayers grown by metal–organic chemical vapor deposition (MOCVD) on 500 nm-thick hydride vapor-phase epitaxy (HVPE) AlN/sapphire templates were investigated. $Al_xGa_{1-x}N$ typically grows under compressive stress on the AlN templates due to its larger lattice parameter, which can lead to increased surface roughness and V-pits in undoped and Ge-doped $Al_xGa_{1-x}N$. The introduction of the group III sources in the growth ambient for a short period of time (5 s) prior to the addition of NH_3 induced a tensile growth stress in the $Al_xGa_{1-x}N$, as measured by in situ wafer curvature measurements, which correlated with an improvement in the surface morphology. However, the pre-metallization was also observed to result in the deposition of a carbon-rich layer at the $Al_xGa_{1-x}N$/AlN interface and an increased density of screw-type dislocations as measured by post-growth x-ray diffraction. By utilizing a pre-metallization step with a lower $Al_xGa_{1-x}N$ growth rate, it was possible to eliminate the carbon interfacial layer and maintain low surface v-pitting and threading dislocation density in Ge-doped $Al_xGa_{1-x}N$. The results provide insight into the impact of pre-metallization on the $Al_xGa_{1-x}N$/AlN interface and the structural properties of the layers.

Keywords Aluminum gallium nitride · electronic materials · heteroepitaxy · MOCVD

Introduction

$Al_XGa_{1-x}N$ has evolved into an important material for ultraviolet (UV) and deep-UV optoelectronics with broad applications in sterilization,[1–4] curing[5,6] etc. as well as solar-blind photodetectors[7,8] and power electronics.[9–11] Since $Al_xGa_{1-x}N$ has both a direct and tunable bandgap, varying the Al composition of the material can cover the range of emission wavelengths from 200 to 365 nm. Development of high-quality $Al_xGa_{1-x}N$ films for device applications, however, has been hampered by several factors including high threading dislocation (TD) densities in epitaxial films grown directly on sapphire or SiC substrates (typically 10^9 cm^{-2} to 10^{10} cm^{-2})[12–14] as well as difficulties achieving *p*-type doping and high *n*-type doping, particularly in high Al fraction ($x > 0.5$) layers.

Several approaches have been developed to produce thick, high-quality AlN templates on sapphire that can serve as substrates for $Al_xGa_{1-x}N$ epitaxy and lead to reduced TD density including low temperature nucleation layers, pulsed atomic layer epitaxy, V/III modulation, migration-enhanced metal–organic chemical vapor deposition (MEMOCVD), flow-modulation metal–organic chemical vapor deposition (MOCVD), epitaxial lateral overgrowth and hydride vapor-phase epitaxy (HVPE).[15–21] HVPE AlN/sapphire templates are now commercially available in 2-inch diameter with reduced TD density (10^8 cm^{-2} to 10^9/cm^{-2}). However, challenges associated with the growth of $Al_xGa_{1-x}N$ on AlN templates remain, including the formation of macro-steps,[22] compositional non-uniformities[23] and point defects[24,25] which degrade the optical properties. Intentional *n*-type doping, with Si or Ge, has further been shown to degrade the structural properties and surface morphology of group III nitrides in general, and particularly for high *n*-type levels which require dopant concentrations on the order of

✉ Joan M. Redwing
jmr31@psu.edu

1 Department of Materials Science and Engineering, The Pennsylvania State University, University Park, PA 16802, USA

2 Materials Research Institute, The Pennsylvania State University, University Park, PA 16802, USA

10^{19} cm^{-3} or more which can lead to increased surface roughness and V-pit formation.[26,27]

The introduction of a short pre-metallization step prior to growth has been shown to improve the surface morphology of undoped $Al_xGa_{1-x}N$ grown by MOCVD on HVPE AlN/sapphire templates.[28] In this case, the group III metalorganic precursors are introduced into the inlet gas for a short time without the presence of NH_3 to achieve metal-rich conditions at the beginning of $Al_xGa_{1-x}N$ growth. Pre-metallization has been shown to reduce the formation of macro-steps and compositional non-uniformities in $Al_xGa_{1-x}N$ as well as cation vacancy (V_{cation})-related point defects.[28,29] Theoretical calculations, for example, demonstrate that the formation energy of V_{cation} is higher under metal-rich compared to N-rich conditions.[29] Consequently, pre-metallization is also anticipated to be beneficial for the growth of *n*-type doped $Al_xGa_{1-x}N$ potentially leading to reduced surface roughness and compensating point defects.

In this study, the effect of pre-metallization was investigated for undoped and Ge-doped $Al_xGa_{1-x}N$ grown by MOCVD on HVPE AlN/sapphire templates. The aim of these studies was to understand if the pre-metallization step would result in a reduction in surface roughness for both undoped and Ge-doped $Al_xGa_{1-x}N$ and what mechanisms lead to tensile stress in the films compared to compressive stress which is typical for $Al_xGa_{1-x}N$ growth on AlN. Additionally, this study sought to explore how growth conditions might be carefully optimized to improve the surface morphology without sacrificing the crystal quality of the $Al_xGa_{1-x}N$ layers.

Experimental Procedure

The $Al_xGa_{1-x}N$ ($x \sim 0.52$–0.56) layers were grown on 1 cm × 1 cm, 500 nm-thick HVPE-AlN/c-plane sapphire templates from nitride solutions. Prior to growth, the AlN/sapphire substrates were cleaned using standard solvents. The epilayer growth was carried out in a vertical cold-wall MOCVD reactor equipped with a k-space multi-beam optical stress (MOS) sensor for in situ wafer curvature measurements. Trimethylaluminum (TMAl), trimethylgallium (TMGa), ultrahigh purity ammonia gas (NH_3), and germane (GeH_4; 2% in H_2) were used as Al, Ga, N and Ge sources, with hydrogen (H_2) as the carrier gas. The reactor pressure and total flow rate were fixed at 6.7 kPa and 8.5 slm, respectively. The AlN template was heated in H_2 to 1250 °C and held for 10 min prior to depositing approximately 500 nm of AlN to reduce the surface roughness. The AlN layers were deposited at a growth rate of 0.5 nm/s using a multi-step growth method, varying V/III ratio, with a TMAl flow rate of 34.5 umol/min and NH_3 flow rates of 44.6, 55.8, 66.9, 78.1, 89.3 mmol/min for each of the steps. The subsequent growth of the $Al_xGa_{1-x}N$ layers (500 nm thick) was conducted after cooling to 1025 °C for 10 min and stabilizing for 5 min. Typically, this cooldown and stabilization step is performed under NH_3 overpressure; however, when introducing the metallization pretreatment, the NH_3 is switched out of the reactor during the 5 min stabilization. Both TMAl and TMGa are switched into the reactor without the NH_3 present and at the same flow rate as the $Al_xGa_{1-x}N$ layer step for 5 s during the metallization pretreatment. The NH_3 is then switched back into the reactor to start the $Al_xGa_{1-x}N$ layer step. Doped $Al_xGa_{1-x}N$ samples were prepared with an initial 100 nm undoped $Al_xGa_{1-x}N$ layer after which GeH_4 was switched into the reactor. A GeH_4/(TMAl + TMGa) ratio of 0.27 was utilized to obtain a carrier concentration of $\sim 1.5 \times 10^{18}/cm^3$ as measured by mercury probe capacitance–voltage measurements. The growth rate of the $Al_xGa_{1-x}N$ was varied from 0.18 to 0.66 nm/s by utilizing TMAl and TMGa flux rates of 13 µmol/min to 21 µmol/min and 9 µmol/min to 19 µmol/min, with minor adjustments to the TMAl/TMGa + TMAl ratio to maintain a constant Al composition in the film. Since both the pre-metallization step and the AlGaN layer were grown using the same flow conditions, references to the growth rate may be understood to be differences in flux as well.

In situ reflectance measurements were used to monitor the growth rate of the AlN and $Al_xGa_{1-x}N$ during the MOCVD process. Changes in film curvature during growth were measured by a multi-beam optical sensor (MOS) and were converted to stress-thickness using a modified version of Stoney's equation.[30] A PANalytical MRD diffractometer was used for high-resolution x-ray diffraction (HRXRD) in a triple-axis geometry to determine the strain and composition of the $Al_xGa_{1-x}N$ film through reciprocal space mapping (RSM) and to estimate the TD density of the films. The x-ray source is a Cu Kα1 radiation line with a wavelength of 0.15406 nm. Screw and edge TD densities were estimated from the full width at half maximum (FWHM) of skew-symmetric scans on $Al_xGa_{1-x}N$. Atomic force microscopy (AFM) surface topography was acquired using a Bruker Icon system in quantitative nanomechanical mapping mode (PeakForce) at room temperature with a PeakForce set point of 2.5 nN and a scan rate of 1 Hz.

The local microstructure of the cross-sectional samples was observed by FEI Titan3 G2 double aberration-corrected microscope at 300 kV. The scanning transmission electron microscope (STEM) images were collected by using a high-angle annular dark field (HAADF) detector which had a collection angle of 52–253 mrad. Energy-dispersive spectrometry (EDS) elemental maps of the sample were collected by using a SuperX EDS system under STEM mode. The thin cross-sectional TEM specimens were prepared by using focused ion beam (FIB, FEI Helios 660) lift-out technique.

Results and Discussion

The effect of the pre-metallization step was initially examined for undoped $Al_xGa_{1-x}N$ grown on the HVPE AlN/sapphire templates. Figure 1a shows the epitaxial structure highlighting the location where the pre-metallization step occurs. A 500 nm-thick homoepitaxial AlN layer was initially grown on the HVPE AlN/sapphire template followed by a 500 nm undoped $Al_xGa_{1-x}N$ layer. To investigate the effect of the pre-metallization step on the stress evolution during the $Al_xGa_{1-x}N$ layer growth, in situ wafer curvature measurements were obtained. Figure 1b compares two samples grown using the same process parameters save for a 5 s pre-metallization step. The incremental stress measured during growth of the two samples is represented by the slope of the stress-thickness versus thickness curve with a negative slope corresponding to a compressive stress and a positive slope indicating a tensile stress. Overall, the stress experienced by the two samples diverge following a similar starting point. For the sample grown without the pre-metallization step, the $Al_xGa_{1-x}N$ layer grows under an initial compressive stress of −8.5 GPa that relaxes slightly to −5.4 GPa after about 50 nm. Compressive stress is typically observed for $Al_xGa_{1-x}N$ growth on AlN and arises from the epitaxial mismatch. The sample with the pre-metallization step, however, grew under a constant tensile stress of 2.2 GPa.

The surface morphologies of the two samples were observed via 10 μm × 10 μm AFM scans as shown in Fig. 1c and d. When the $Al_xGa_{1-x}N$ layer was grown under compressive stress without a pre-metallization step, the $Al_xGa_{1-x}N$ surface exhibits texture consistent with an island growth mode seen in other referenced work and has an increased surface roughness (RMS 2.38 nm).[31] Introducing the pre-metallization step reduces the island height and corresponding surface roughness to 1.70 nm RMS. This change in the surface morphology which correlates to a change from compressive to tensile stress suggests that the pre-metallization step is altering the initial nucleation of $Al_xGa_{1-x}N$ on the AlN surface. It is worth noting that for both samples, the surface morphology does not show evidence of step-bunching or macro-steps propagating from the underlying HVPE AlN template layer, which may be a result of the added AlN homoepitaxial layer.[28]

RSM measurements were undertaken to study and compare the Al composition and extent of strain relaxation of the

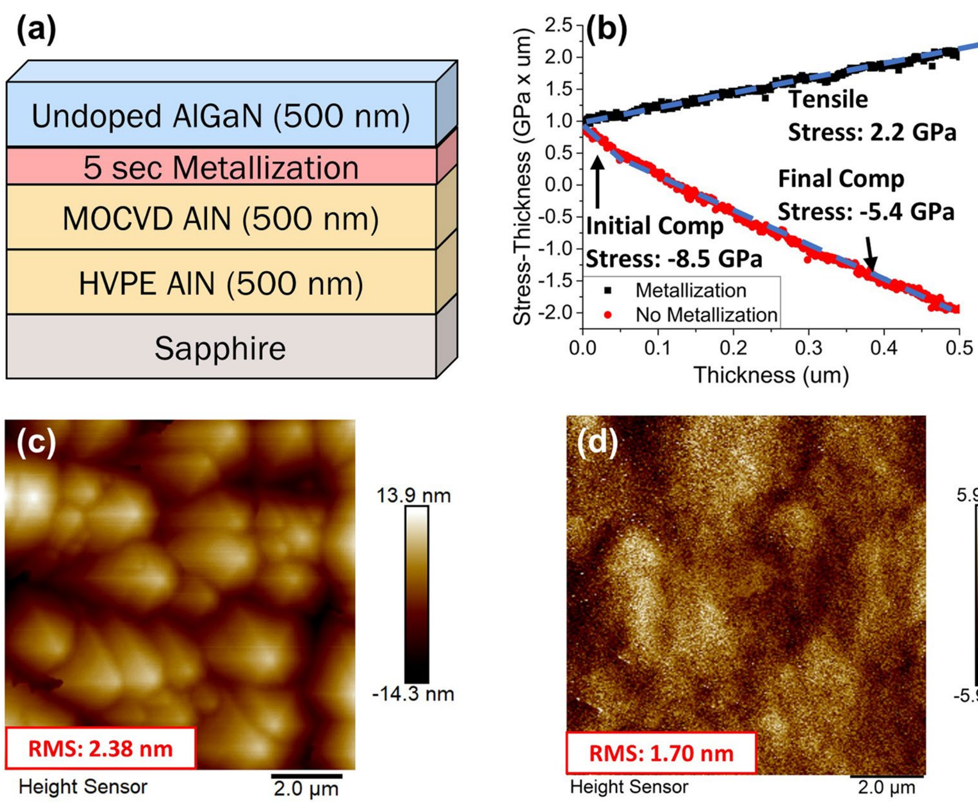

Fig. 1 (a) Schematic illustration of the layer structure showing the location of the pre-metallization step. (b) Stress thickness versus thickness of $Al_{0.5}Ga_{0.5}$ N obtained from in situ stress measurements on samples growth with and without the pre-metallization step at a growth rate of 0.63 nm/s. (c) and (d) are the AFM images (10 μm × 10 μm) of the $Al_{0.5}Ga_{0.5}$ N surface without and with the pre-metallization step, respectively.

$Al_xGa_{1-x}N$ layers. Because of the accuracy of RSM measurements, they are commonly used to extract compositional information from an asymmetric scan. Figure 2a and b show the $\left(10\bar{1}4\right)$ asymmetric plane RSMs of $Al_xGa_{1-x}N$ samples grown without and with the 5 s pre-metallization step, respectively. In the RSM, the top contour represents the AlN layer on the sapphire substrate, while the $Al_xGa_{1-x}N$ layer contour is at the bottom. The two $Al_xGa_{1-x}N$ layers were found to have Al fractions of 56% and 52% for the samples grown without and with the pre-metallization step, respectively. The increased Al fraction in the $Al_xGa_{1-x}N$ grown without pre-metallization is attributed to the compositional pulling effect which has previously been shown to increase Al incorporation in compressively strained $Al_xGa_{1-x}N$ films.[32]

For the $Al_xGa_{1-x}N$ sample grown without pre-metallization, the $Al_xGa_{1-x}N$ and AlN contours nearly align vertically indicating that a high level of compressive strain remains in the $Al_xGa_{1-x}N$ film; extracting the relaxation yields a value of 36.4%. This value correlates well to the MOS data obtained on this sample (Fig. 1b), where the compressive stress was observed to decrease from −8.5 GPa initially to −5.4 GPa, indicating a relaxation of ~ 36.5%. For the $Al_xGa_{1-x}N$ sample grown with pre-metallization (Fig. 2b), the $Al_xGa_{1-x}N$ contour is offset significantly from the AlN contour indicating a low level of strain present. Extracting the relaxation for this sample yields a value of 100%, i.e. the compressive strain in the $Al_xGa_{1-x}N$ film is fully relaxed, consistent with the tensile stress measured during growth (Fig. 1b). It should be noted that this method also provides insight into the crystal quality (e.g. extent of twist/tilt, defects and dislocations) of strain-relaxed heterostructures from the diffuse scattering around the reflection peaks. The diffuse nature of the $Al_xGa_{1-x}N$ contour in Fig. 2b indicates that the relaxation is accompanied by a reduction in crystal quality for the $Al_xGa_{1-x}N$ grown with pre-metallization compared to the sample grown without pre-metallization (Fig. 2a).

X-ray rocking curve (XRC) measurements were performed to further understand the relationship between the stress evolution and structural quality of the undoped $Al_xGa_{1-x}N$ films. During the growth, TDs are formed to alleviate the strain caused by the twist and tilt misorientation of subgrains. The TDs associated with tilt misorientation are screw-type while the TDs associated with twist misorientation are edge type. Using the full width at half maximum (FWHM) of the (0002) and $\left(10\bar{1}0\right)$ reflections, the screw-type and edge-type dislocation densities can be extracted.[33] Using a standard four-circle diffractometer XRD setup, the (0002) reflection is straightforward to measure. However, the $\left(10\bar{1}0\right)$ reflection is difficult to measure directly without a synchrotron x-ray source as beam attenuation is an issue for transmission methods and in-plane methods have limited penetration depth (~ 10 nm). It is therefore common to use a series of skew-symmetric ω-scans that are only sensitive to twist or reflections occurring at high χ angles such that the FWHM is predominately composed of twist misorientation.

Applying the method developed by Srikant et al.,[34] the extrapolation of the $\left(10\bar{1}0\right)$ FWHM can be obtained by measuring several reflections of increasing inclination angle as seen in Fig. 3. Once both the tilt and twist FWHM are determined, the threading dislocation density (ρ) for each type can be calculated using the classical model for randomly distributed dislocations[35]:

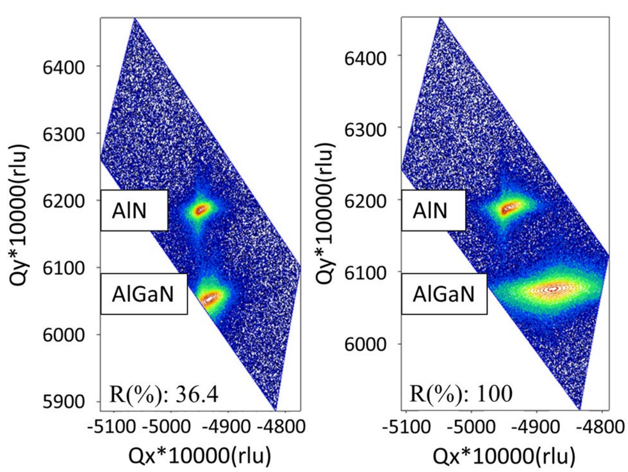

Fig. 2 Reciprocal space maps of the (104) plane of undoped $Al_{0.5}Ga_{0.5}$ N grown on the HVPE AlN/sapphire templates (a) without and (b) with a 5 s pre-metallization step.

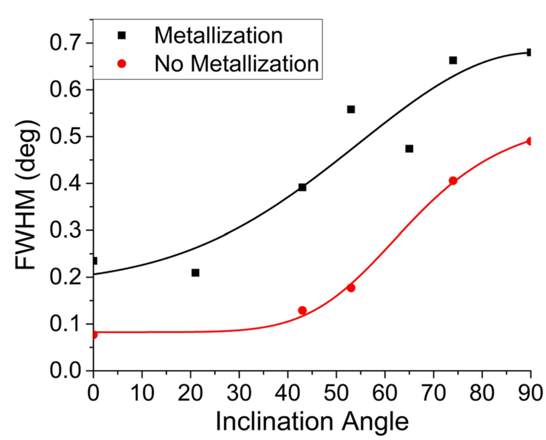

Fig. 3 XRC FWHM of reflections as a function of inclination angle to extrapolate the tilt and twist in the AlGaN films with (black squares) and without (red circles) the pre-metallization step (Color figure online).

$$\rho_{screw} = \frac{\tau_{tilt}^2}{4.36 b_{screw}^2}$$

$$\rho_{edge} = \frac{\tau_{twist}^2}{4.36 b_{edge}^2}$$

where τ_{tilt} and τ_{twist} are the FWHMs of the (0002) and $\left(10\overline{1}0\right)$ scans and the b_{screw} and b_{edge} are the Burgers vectors calculated from the lattice parameters of each sample taking into account their specific compositions.

Figure 3 and Table I provide a comparison of the TD densities for the $Al_xGa_{1-x}N$ grown with and without the pre-metallization step and the AlN underlayers. The results demonstrate an order of magnitude increase in the screw-type TD density for the $Al_xGa_{1-x}N$ grown with the pre-metallization step as well as a threefold increase in edge-type TD density. The increase in the TD density resulting from the pre-metallization step is consistent with the broadening and full relaxation of compressive strain obtained from the RSM measurements (Fig. 2), and is largely independent of the dislocation density of the underlying AlN layer, showing higher screw-type dislocations despite a reduction of the same defect type. As reported by Romanov and Speck,[36] inclination of TDs in $Al_xGa_{1-x}N$ gives rise to a strain gradient during growth that relaxes compressive stress. However, this alone would not account for the tensile stress experienced in the $Al_xGa_{1-x}N$ layer. The higher TD density in the $Al_xGa_{1-x}N$ grown with pre-metallization though, would explain the tensile growth stress measured by MOS (Fig. 1). The magnitude of the strain gradient is proportional to the TD density hence a larger strain gradient is expected for the $Al_xGa_{1-x}N$ grown with the pre-metallization step leading to the measured tensile stress during growth.

The addition of dopants can also impact the film stress and surface morphology of $Al_xGa_{1-x}N$. Silicon doping induces TD inclination generating tensile strain in $Al_xGa_{1-x}N$ films via an effective climb mechanism.[36,37] In contrast, Ge doping does not alter the film stress of $Al_xGa_{1-x}N$ and was therefore selected as the *n*-type dopant in this study.[38] To investigate the effect of pre-metallization on the growth of Ge-doped $Al_xGa_{1-x}N$, additional samples were prepared with a similar layer structure to Fig. 1a but adding GeH_4 during growth of the $Al_xGa_{1-x}N$ layer. In the samples grown with a 5 s pre-metallization, the growth rate (GR) of the $Al_xGa_{1-x}N$ was varied as 0.63 nm/s (fast GR), 0.48 nm/s (medium GR) and 0.18 nm/s (slow GR) by varying the TMAl and TMGa flow rates while keeping the overall TMAl/(TMAl + TMGa) ratio approximately constant. An additional sample was grown using a fast GR (0.66 nm/s) but without pre-metallization.

The addition of Ge during the fast growth rate results in the formation of V-pits (Fig. 4e) leading to a significantly increased surface roughness (RMS = 8.32 nm) compared to the undoped $Al_xGa_{1-x}N$ (Fig. 1c) at a similar fast growth rate, which has RMS = 2.38 nm. The stress-thickness curve (Fig. 4a), however, indicates that this Ge-doped film grows under a compressive stress, similar to the undoped $Al_xGa_{1-x}N$ (Fig. 1b), and consistent with prior reports.[38] The addition of the 5 s pre-metallization step significantly reduces the density of V-pits and the overall surface roughness (RMS ~ 2 nm) for the Ge-doped $Al_xGa_{1-x}N$ films grown with fast and medium growth rates (Fig. 4b and c). A significant change is that the $Al_xGa_{1-x}N$ grows under a tensile stress in this case (Fig. 4a), consistent with an increase in both edge and screw-type TDs resulting from the pre-metallization step (Table II), as also observed for the undoped $Al_xGa_{1-x}N$ (Fig. 1b) at similar growth rates. Further reducing the $Al_xGa_{1-x}N$ growth rate to 0.18 nm/s, however, preserves the compressive growth stress in the Ge-doped $Al_xGa_{1-x}N$ while maintaining reduced V-pits and a lower surface roughness (RMS 4.25 nm). Since the pre-metallization time was held constant for this series of samples, the reduction in growth rate would also lead to reduced exposure of the surface to the metal precursors prior to AlGaN growth.

Cross-sectional $Al_xGa_{1-x}N$ films were studied by using the HAADF STEM imaging technique and EDS mapping to observe the dislocation microstructure and elemental composition in the epitaxial films. Figure 5a and b show the HAADF STEM images from the $\langle 1\overline{1}00\rangle$ zone axis, revealing the effect of the pre-metallization step on the TDs in the $Al_xGa_{1-x}N$ layer. A combination of edge (*a* type), screw (*c* type) and mixed (a/c type) dislocations are present in the Ge-doped $Al_xGa_{1-x}N$ films. Inclined TDs are clearly present in the sample grown without pre-metallization (Fig. 5a), which is consistent with the compressive growth stress measured via MOS (Fig. 4a). Conversely, the sample grown with a 5 s

Table I Estimated TD densities of AlGaN and AlN as calculated by HR-XRD

		Screw ρ_{TD}, cm^{-2}	Edge ρ_{TD}, cm^{-2}	Total ρ_{TD}, cm^{-2}
AlGaN on AlN without pre-metallization	AlGaN	1.58×10^8	1.13×10^{10}	1.15×10^{10}
	AlN	4.75×10^7	4.63×10^9	4.68×10^9
AlGaN on AlN with pre-metallization	AlGaN	1.46×10^9	3.02×10^{10}	3.17×10^{10}
	AlN	3.16×10^7	4.64×10^9	4.67×10^9

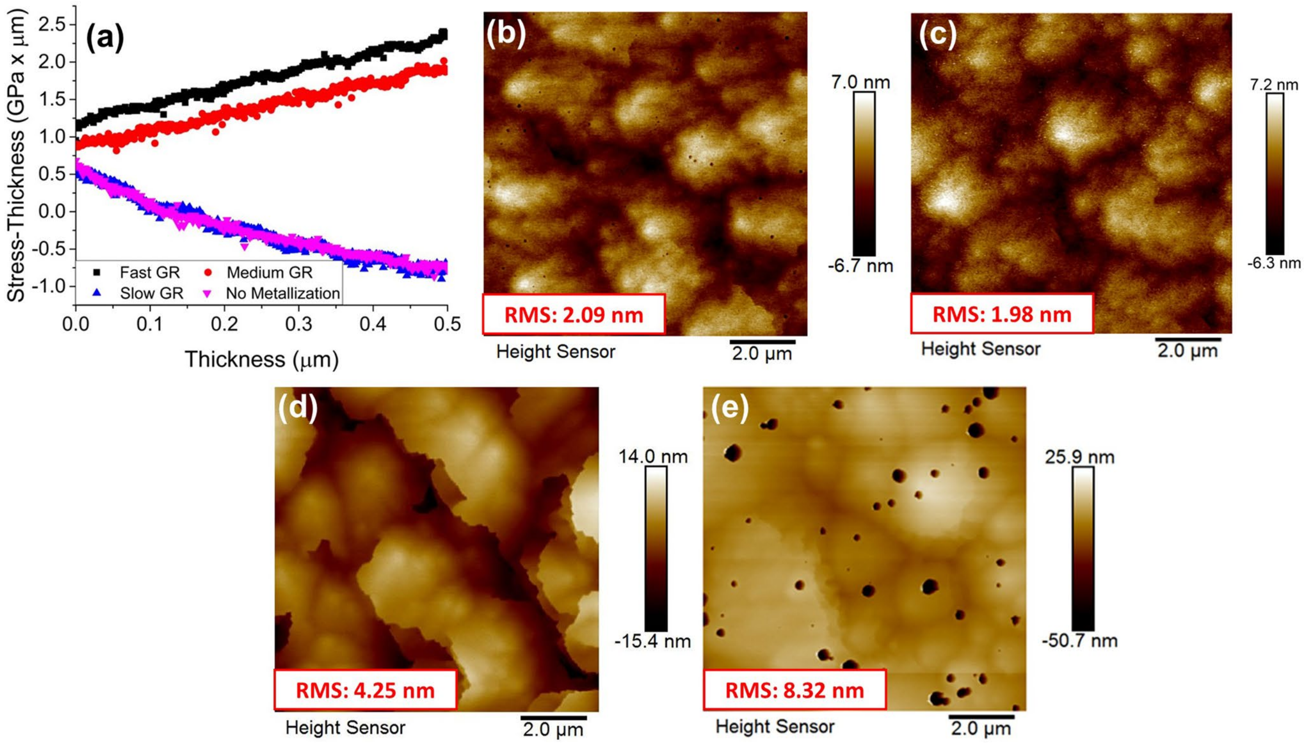

Fig. 4 (a) Stress-thickness versus thickness plots of Ge-doped AlGaN as a function of growth rate (GR) using a 5 s pre-metallization and without pre-metallization. Corresponding AFM images (10 μm × 10 μm) of the Ge-doped AlGaN samples with (b) fast GR (0.63 nm/s), (c) medium GR (0.48 nm/s) (d) slow GR (0.18 nm/s) and (e) with fast GR (0.66 nm/s) but without pre-metallization.

Table II Estimated TD densities of Ge-doped AlGaN and AlN as calculated by HR-XRD

			Screw ρ_{TD}, cm^{-2}		Edge ρ_{TD}, cm^{-2}		Total ρ_{TD},cm^{-2}	
Ge-AlGaN on AlN under compression	AlGaN	AlN	2.03×10^{8}	7.23×10^{7}	1.33×10^{10}	2.52×10^{9}	1.35×10^{10}	2.59×10^{9}
Ge-AlGaN on AlN under tension	AlGaN	AlN	1.50×10^{9}	3.10×10^{7}	1.02×10^{10}	1.52×10^{9}	1.17×10^{10}	1.55×10^{9}

pre-metallization and fast GR exhibits a higher TD density and negligible bending of TDs (Fig. 5b), consistent with the measured tensile growth stress (Fig. 4a). It can also be observed in both samples that some of the screw TDs present in the underlying AlN layer propagate through the interface, contributing to the overall TD density in the $Al_xGa_{1-x}N$ film. For the film grown with 5 s pre-metallization and a fast GR, EDS mapping reveals the presence of a high level of carbon impurities at the $Al_xGa_{1-x}N$/AlN interface (Fig. 5c) along with increased Al directly above the carbon-rich layer. The carbon layer arises from pyrolysis of the TMAl and TMGa during the pre-metallization step when the metal–organic precursors are present in the growth ambient without NH_3. Even though H_2 is used as the carrier gas, atomic hydrogen from NH_3 decomposition is needed to effectively remove carbon from the metalorganic sources from the growth surface. The fast GR employed leads to excess carbon that cannot be efficiently removed prior to growth of the $Al_xGa_{1-x}N$ layer. The carbon-rich layer disrupts heteroepitaxy leading to significantly increased TD density and tensile growth stress. These conditions also result in elimination of V-pits on the surface, which form in response to relaxation of compressive stress,[26] leading to an overall reduction in surface roughness. The Al-rich layer above the carbon may arise from Al deposition and desorption of Ga from the surface given the 1025 °C temperature.

Similar characterization was carried out on the Ge-doped $Al_xGa_{1-x}N$ grown with 5 s pre-metallization but a

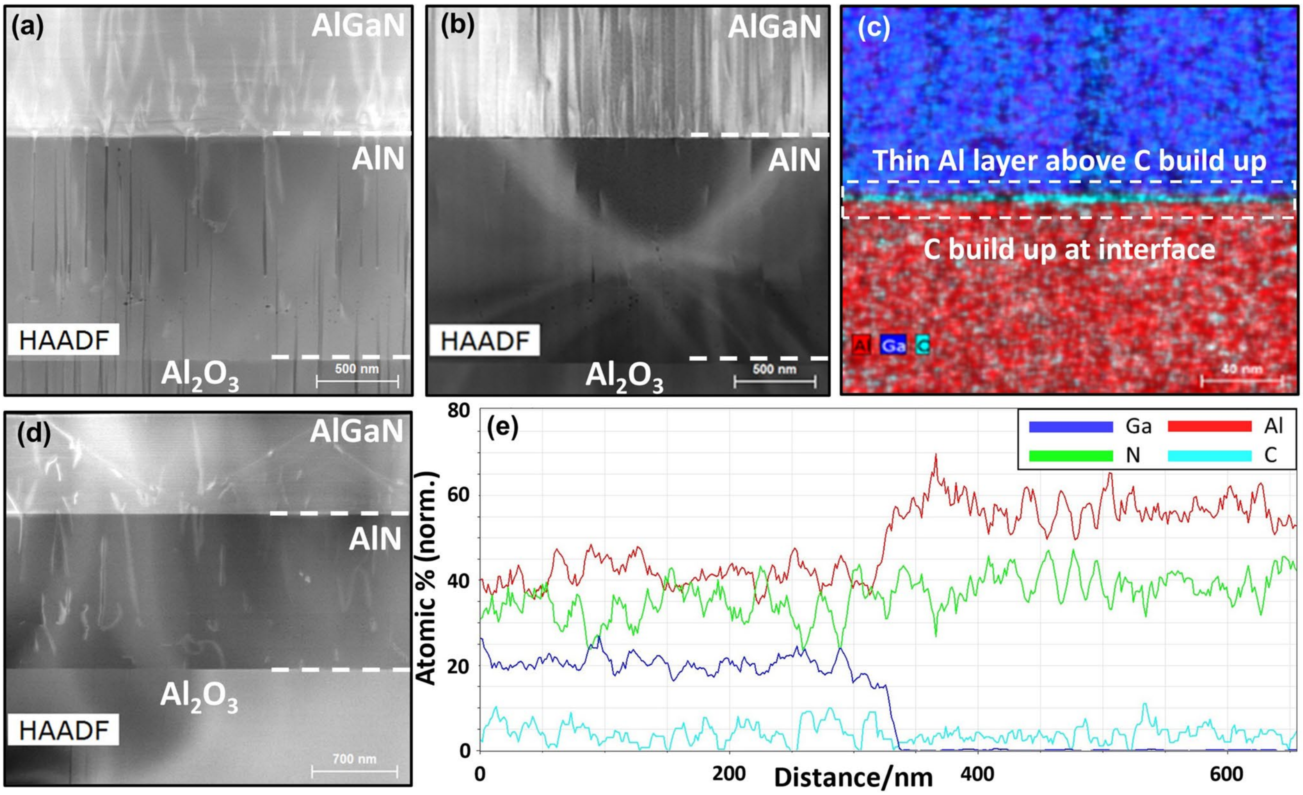

Fig. 5 (a) STEM micrograph of the AlGaN dislocation structure on an AlN layer grown without the pre-metallization step (b) STEM micrograph of the AlGaN dislocation structure on an AlN layer grown with a 5 s pre-metallization step (c) EDS mapping of the 5 s pre-metallization step AlGaN/AlN interface showing a buildup of C but also the presence of Al prior to AlGaN growth. (d) STEM micrograph of the dislocation structure for the low flux 5 s pre-metallization step AlGaN/AlN interface. (e) EDS line scans cross the AlGaN/AlN interface shown in (d) highlighting the absence of carbon buildup (Color figure online).

slow GR. In this case, the HAADF STEM image reveals evidence of TD inclination (Fig. 5d) and an EDS line scan indicates negligible excess carbon at the $Al_xGa_{1-x}N$/AlN interface (Fig. 5e), similar to the results obtained without the pre-metallization step. However, the surface of this sample (Fig. 4d) is largely free of V-pits and has a lower RMS roughness than the sample grown without pre-metallization (Fig. 4e) demonstrating the beneficial effects of a short pre-metallization step as previously reported.[28] These results demonstrate the importance of careful tuning of the pre-metallization process to avoid carbon incorporation at the interface which compromises the overall crystal quality of the $Al_xGa_{1-x}N$ layers.

Conclusions

In this work, the influence of a pre-metallization step prior to $Al_xGa_{1-x}N$ epitaxy on HVPE AlN/sapphire templates was investigated. The pre-metallization step was shown to induce a tensile growth stress in the $Al_xGa_{1-x}N$ compared to compressive stress which is typically observed for $Al_xGa_{1-x}N$/AlN heteroepitaxy. This correlated with reduced surface roughness in undoped $Al_xGa_{1-x}N$ and reduced v-pitting in Ge-doped $Al_xGa_{1-x}N$. However, the use of pre-metallization also resulted in deposition of a carbon-rich interfacial layer and an increased density of screw-type dislocations in the $Al_xGa_{1-x}N$. By decreasing the group III precursor flow rate and hence the $Al_xGa_{1-x}N$ growth rate, it was possible to eliminate the carbon-rich layer and the increase in dislocation density while maintaining the beneficial aspects of pre-metallization including reduced surface roughness and V-pit density. These results provide additional insights into the effect of pre-metallization on film stress and the structural properties of undoped and Ge-doped $Al_xGa_{1-x}N$.

Acknowledgments Financial support for this project was provided by AFOSR under Award FA9550-19-1-0349.

Conflict of interest The authors declare that they have no known competing financial interests or personal relationships that could have appeared to influence the work reported in this paper.

References

1. Surapong Rattanakul and Kumiko Oguma, Inactivation kinetics and efficiencies of UV-LEDs against Pseudomonas aeruginosa, legionella pneumophila, and surrogate microorganisms. *Water Res.* 130, 31 (2018).
2. S. Rattanakul and K. Oguma, Analysis of hydroxyl radicals and inactivation mechanisms of bacteriophage MS2 in response to a simultaneous application of UV and chlorine. *Environ. Sci. Technol.* 51, 455 (2017).
3. X. Zhou, Z. Li, J. Lan, Y. Yan, and N. Zhu, Kinetics of inactivation and photoreactivation of Escherichia coli using ultrasound-enhanced UV-C light-emitting diodes disinfection. *Ultrason. Sonochem.* 35, 471 (2017).
4. L.W. Gassie and J.D. Englehardt, Advanced oxidation and disinfection processes for onsite net-zero greywater reuse: A review. *Water Res.* 125, 384 (2017).
5. H. Okamura, S. Niizeki, T. Ochi, and A. Matsumoto, UV curable formulations for UV-C LEDs. *J. Photopolym. Sci. Technol.* 29, 99 (2016).
6. H. Okamura, T. Matoba, K. Takada, M. Yamashita, M. Shirai, and A. Matsumoto, Photo-thermal dual curing of acrylic anchor resins for screen printing. *Prog. Org. Coat.* 100, 47 (2016).
7. Cai Qing, Haifan You, Hui Guo, Jin Wang, Bin Liu, Zili Xie, Dunjun Chen, Lu. Hai, Youdou Zheng, and Rong Zhang, Progress on AlGaN-based solar-blind ultraviolet photodetectors and focal plane arrays. *Light Sci. Appl.* 10, 1 (2021).
8. U. Varshney, N. Aggarwal, and G. Gupta, Current advances in solar-blind photodetection technology: Using Ga2O3 & AlGaN. *J. Mater. Chem. C* 1, 1 (2022).
9. Liu Tang, Bo. Tang, Hong Zhang, and Yinmei Yuan, Review of research on AlGaN MOCVD growth. *ECS J. Solid State Sci. Technol.* 9, 024009 (2020).
10. S. Rahman, S.W.M. Hatta, and N. Soin, Analytical optimization of AlGaN/GaN/AlGaN DH-HEMT device performance based on buffer characteristics. *ECS J. Solid State Sci. Technol.* 8, 165 (2019).
11. R.J. Kaplar, Andrew A. Allerman, A.M. Armstrong, Mary H. Crawford, Jeramy Ray Dickerson, Arthur J. Fischer, A.G. Baca, and E.A. Douglas, Ultra-wide-bandgap AlGaN power electronic devices. *ECS J. Solid State Sci. Technol.* 6, 3061 (2016).
12. Follstaedt David Martin, Stephen Roger Lee, P.P. Provencio, A.A. Allerman, J.A. Floro, and M.H. Crawford, Relaxation of compressively-strained AlGaN by inclined threading dislocations. *Appl. Phys. Lett.* 87, 121112 (2005).
13. Fabio Alessio Marino, Nicolas Faralli, Tomas Palacios, David K. Ferry, Stephen M. Goodnick, and Marco Saraniti, Effects of threading dislocations on AlGaN/GaN high-electron mobility transistors. *IEEE Transact. Elect. Dev.* 57, 353 (2009).
14. S.R. Lee, A.M. West, A.A. Allerman, K.E. Waldrip, D.M. Follstaedt, Paula Polyak Provencio, D.D. Koleske, and C.R. Abernathy, Effect of threading dislocations on the Bragg peakwidths of GaN, AlGaN, and AlN heterolayers. *Appl. Phys. Lett.* 86, 241904 (2005).
15. Hiroshi Amano, N. Sawaki, I. Akasaki, and Y. Toyoda, Metalorganic vapor phase epitaxial growth of a high quality GaN film using an AlN buffer layer. *Appl. Phys. Lett.* 48, 353 (1986).
16. J.P. Zhang, V. Adivarahan, H.M. Wang, Q. Fareed, E. Kuokstis, A. Chitnis, M. Shatalov, J.W. Yang, G. Simin, M.A. Khan, and M. Shur, Quaternary AlInGaN multiple quantum wells for ultraviolet light emitting diodes. *Jpn. J. Appl. Phys.* 40, 921 (2001).
17. M. Imura, K. Nakano, N. Fujimoto, N. Okada, K. Balakrishnan, M. Iwaya, S. Kamiyama, H. Amano, I. Akasaki, T. Noro, and T. Takagi, High-temperature metal-organic vapor phase epitaxial growth of AlN on sapphire by multi transition growth mode method varying V/III ratio. *Jpn. J. Appl. Phys.* 45, 8639 (2006).
18. RS Qhalid. Fareed, R. Jain, R. Gaska, M.S. Shur, J. Wu, W. Walukiewicz, and M. Asif Khan, High quality InN/GaN heterostructures grown by migration enhanced metalorganic chemical vapor deposition. *Appl. Phys. Let.* 84, 1892 (2004).
19. M. Takeuchi, H. Shimizu, R. Kajitani, K. Kawasaki, T. Kinoshita, K. Takada, H. Murakami, Y. Kumagai, A. Koukitu, T. Koyama, and S.F. Chichibu, Al-and N-polar AlN layers grown on c-plane sapphire substrates by modified flow-modulation MOCVD. *J. Cryst. Growth* 305, 360 (2007).
20. S. Nakamura, M. Senoh, S.I. Nagahama, N. Iwasa, T. Yamada, T. Matsushita, H. Kiyoku, Y. Sugimoto, T. Kozaki, H. Umemoto, and M. Sano, Present status of InGaN/GaN/AlGaN-based laser diodes. *J. Cryst. Growth* 189, 820 (1998).
21. A. Knauer, V. Kueller, U. Zeimer, M. Weyers, C. Reich, and M. Kneissl, AlGaN layer structures for deep UV emitters on laterally overgrown AlN/sapphire templates. *Phys. Status Solidi A* 210, 451 (2013).
22. Gunnar Kusch, Haoning Li, Paul R. Edwards, Jochen Bruckbauer, Thomas C. Sadler, Peter J. Parbrook, and Robert W. Martin, Influence of substrate miscut angle on surface morphology and luminescence properties of AlGaN. *Appl. Phys. Lett.* 104, 092114 (2014).
23. I. Bryan, Z. Bryan, S. Mita, A. Rice, L. Hussey, C. Shelton, J. Tweedie, J.-P. Maria, R. Collazo, and Z. Sitar, The role of surface kinetics on composition and quality of AlGaN. *J. Cryst. Growth* 451, 65 (2016).
24. S.F. Chichibu, H. Miyake, K. Hiramtsu, and A. Uedono, Impacts of dislocations and point defects on the internal quantum efficiency of the near-band-edge emission in AlGaN-Based DUV Light-emitting materials. *III-Nitride Ultrav. Emitt.* 227, 115 (2016).
25. S.F. Chichibu, H. Miyake, Y. Ishikawa, M. Tashiro, T. Ohtomo, K. Furusawa, K. Hazu, K. Hiramatsu, and A. Uedono, Impacts of Si-doping and resultant cation vacancy formation on the luminescence dynamics for the near-band-edge emission of $A_{l0.6}Ga_{0.4}N$ films grown on AlN templates by metalorganic vapor phase epitaxy. *J. Appl. Phys.* 113, 213506 (2013).
26. P. Cantu, F. Wu, P. Waltereit, S. Keller, A.E. Romanov, U.K. Mishra, S.P. DenBaars, and J.S. Speck, Si doping effect on strain reduction in compressively strained $A_{l0.49}Ga_{0.5}1$ N thin films. *Appl. Phys. Lett.* 83, 674 (2003).
27. N.G. Young, R.M. Farrell, M. Iza, S. Nakamura, S.P. DenBaars, C. Weisbuch, and J.S. Speck, Germanium doping of GaN by metalorganic chemical vapor deposition for polarization screening applications. *J. Cryst. Growth* 455, 105 (2016).
28. Ke. Jiang, Xiaojuan Sun, Jianwei Ben, Zhiming Shi, Yuping Jia, Wu. You, Cuihong Kai, Yong Wang, and Dabing Li, Suppressing the compositional non-uniformity of AlGaN grown on a HVPE-AlN template with large macro-steps. *Cryst. Eng. Comm.* 21, 4864 (2019).
29. Ke. Jiang, X. Sun, J. Ben, Z. Shi, Y. Jia, Y. Chen, S. Zhang, Wu. Tong, W. Lü, and D. Li, Suppressing the luminescence of Vcation-related point-defect in AlGaN grown by MOCVD on HVPE-AlN. *Appl. Surf. Sci.* 520, 146369 (2020).
30. Stoney, George Gerald. The tension of metallic films deposited by electrolysis. In: *Proceedings of the Royal Society of London. Series A, Containing Papers of a Mathematical and Physical Character*. 82(553): 172 (1909).
31. B. Liu, F. Xu, J. Wang, J. Lang, L. Wang, X. Fang, X. Yang, X. Kang, X. Wang, Z. Qin, and W. Ge, Correlation between electrical properties and growth dynamics for Si-doped Al-rich AlGaN grown by metal-organic chemical vapor deposition. *Micro Nanostruct.* 163, 107141 (2022).

32. B. Liu, R. Zhang, J.G. Zheng, X.L. Ji, D.Y. Fu, Z.L. Xie, D.J. Chen, P. Chen, R.L. Jiang, and Y.D. Zheng, Composition pulling effect and strain relief mechanism in AlGaN/AlN distributed Bragg reflectors. *Appl. Phys. Lett.* 98, 261916 (2011).
33. M.A. Moram and M.E. Vickers, X-ray diffraction of III-nitrides. *Rep. Prog. Phys.* 72, 036502 (2009).
34. V. Srikant, J.S. Speck, and D.R. Clarke, Mosaic structure in epitaxial thin films having large lattice mismatch. *J. of Appl. Phys.* 82, 4286 (1997).
35. C.G. Dunn and E.F. Kogh, Comparison of dislocation densities of primary and secondary recrystallization grains of Si-Fe. *Acta Metall.* 5, 548 (1957).
36. A.E. Romanov and J.S. Speck, Stress relaxation in mismatched layers due to threading dislocation inclination. *Appl. Phys. Lett.* 83, 2569 (2003).
37. David M. Follstaedt, Stephen R. Lee, Andrew A. Allerman, and J.A. Floro, Strain relaxation in AlGaN multilayer structures by inclined dislocations. *J. Appl. Phys.* 105, 083507 (2009).
38. Anushka Bansal, Ke. Wang, James Spencer Lundh, Sukwon Choi, and Joan M. Redwing, Effect of Ge doping on growth stress and conductivity in $Al_xGa_{1-x}N$. *Appl. Phys. Lett.* 114, 142101 (2019).